Journal of Materials Science: Materials in Electronics (2019) 30:13785–13796
https://doi.org/10.1007/s10854-019-01762-7

Synergistically enhanced photocatalytic performance of $Bi_4Ti_3O_{12}$ nanosheets by Au and Ag nanoparticles

Xinxin Zhao[1] · Hua Yang[1] · Ziming Cui[1] · Zao Yi[2] · Hui Yu[3]

Received: 1 November 2018 / Accepted: 26 June 2019 / Published online: 28 June 2019

Abstract
In this work, we attempted to assemble Au and Ag nanoparticles (NPs) with different sizes onto $Bi_4Ti_3O_{12}$ (BTO) nanosheets with the aim of synergistically enhancing the photocatalytic performance. The as-prepared Au–Ag@BTO composite was systematically characterized by means of TEM, XRD, XPS, FTIR, UV–vis DRS, PL spectroscopy, EIS and photocurrent spectroscopy. The TEM observation demonstrates that larger-sized Au NPs (average size: 20 nm) and smaller-sized Ag NPs (average size: 8 nm) are uniformly decorated on the surface of BTO nanosheets. Compared to bare BTO, the Au–Ag@BTO composite manifests an increased visible light absorption, increased bandgap, increased photocurrent density, decreased charge-transfer resistance and decreased PL intensity. Separately using simulated sunlight, UV light and visible light as the light source, the photocatalytic performance of the composite was evaluated by the degradation of RhB. An enhanced photocatalytic performance of the composite is observed in all the cases. Under UV irradiation, the photocatalytic enhancement is mainly ascribed to the efficient separation of photogenerated electron/hole pairs caused by the smaller-sized Ag NPs, whereas the photocatalytic enhancement under visible light irradiation is dominantly due to the LSPR effects of the larger-sized Au NPs. The synergistic photocatalytic enhancement between Ag and Au NPs is achieved under simulated sunlight irradiation. Active species trapping experiments were carried out, revealing that photogenerated holes and $\cdot O_2^-$ radicals play a dominant and secondary role in the photocatalysis, respectively.

1 Introduction

Nowadays, environmental pollution is getting more and more serious and becoming one of the greatest problems facing mankind. In particular, the rapidly developing chemical industries (*e.g.* textile, leather, paper, paint, cosmetic and oil manufacturers) generate a huge amount of wastewater containing more than one million tons of organic dyes worldwide annually [1]. The organic pollutants must be removed or decomposed before the wastewater is discharged into water bodies, because most of them are carcinogenic and pose a tremendous threat to aquatic life and human health. Under the condition of energy shortage, how to use solar energy as the power source to decompose organic pollutants has become an important subject. To achieve this aim, semiconductor-based photocatalysis has recently aroused a tremendous interest [2–5]. When a semiconductor is irradiated with sunlight, electrons (e^-) are excited from the valence band (VB) to the conduction band (CB), simultaneously creating holes (h^+) in the VB. The photocatalytic degradation of organic pollutants is highly associated with the photogenerated electrons and holes. Nevertheless, for most of the famous semiconductor photocatalysts (*e.g.* TiO_2, $SrTiO_3$, $CaTiO_3$, $Bi_4Ti_3O_{12}$ [6–9]), the solar energy utilization rate is generally very low since they can only absorb ultraviolet (UV) due to their large bandgap ($E_g > 3.0$ eV). Further, the photogenerated electron/hole pairs in bare semiconductors easily undergo rapid geminate recombination, thus making their photocatalytic activity limited. To efficiently separate

Electronic supplementary material The online version of this article (https://doi.org/10.1007/s10854-019-01762-7) contains supplementary material, which is available to authorized users.

✉ Hua Yang
hyang@lut.cn

[1] State Key Laboratory of Advanced Processing and Recycling of Non-ferrous Metals, Lanzhou University of Technology, Lanzhou 730050, China

[2] Joint Laboratory for Extreme Conditions Matter Properties, Southwest University of Science and Technology, Mianyang 621010, China

[3] School of Chemistry & Environmental Engineering, Changchun University of Science and Technology, Changchun 130022, China

the photoexcited electron/hole pairs is one of the most crucial points to achieve excellent photocatalyticperformance of semiconductors [10–13].

Graphene and noble metal nanoparticles (NPs), owing to their intriguing physicochemical properties [14–18], have been widely used as the modifiers to improve the photocatalytic performances of semiconductor photocatalysts [19–23]. The enhanced photocatalytic activity by the decoration with noble metal NPs is generally ascribed to two mechanisms [22, 23]. First, noble metal NPs can act as electron sinks to trap photogenerated electrons from the semiconductor, thus leading to an efficient separation of electron/hole pairs. Second, noble metal NPs can induce localized surface plasmon resonance (LSPR) by absorbing visible light with wavelengths corresponding to their plasmonic absorption bands [24–26]. The electromagnetic field caused by LSPR can facilitate the generation and separation of electron/hole pairs in the semiconductor. Simultaneously, LSPR-induced electron/hole pairs in noble metal NPs could also participate in the photocatalytic reactions. The two mechanisms depend highly on the size of noble metal NPs, that is, smaller-sized noble metal NPs mainly act as electron sinks, whereas larger-sized noble metal NPs dominantly behave as LSPR effects [22, 23]. Although much recent work has been devoted to the development of noble metal decorated photocatalysts, little research has been concerned with the synergistic effect between two types of noble metal NPs with different sizes.

Bismuth titanate ($Bi_4Ti_3O_{12}$, BTO) is an important semiconductor photocatalyst, exhibiting powerful photocatalytic activity toward the degradation of organic pollutants as well as water splitting into hydrogen [27–34]. BTO has a special layer structure with perovskite-like $(Bi_2Ti_3O_{10})^{2-}$ blocks alternated by $(Bi_2O_2)^{2+}$ units along the b-axis ([010] direction). The formed polarization electric field (or internal electric field) perpendicular to the (010) facet easily drives the separation and migration of photogenerated electrons and holes along the [010] direction to reach the (010) facet [35]. This implies that the (010) facet could be the highly photocatalytically active facet. In our previous work, we have synthesized large-sized BTO nanosheets with nearly 100% exposed (010) facet via a hydrothermal route and found that they exhibited a photocatalytic activity much superior to that of BTO nanoparticles [27]. More recently some work has been concerned with the decoration of Ag or Au NPs onto the surface of BTO nanostructures with the aim of enhancing the photocatalytic performance [36–38]. The enhanced photocatalytic mechanism was explained by electron capture or LSPR effect of the noble metal NPs. To the best of our knowledge, however, there is no research devoted to the decoration of two types of noble metal NPs with different sizes onto BTO photocatalyst. In this work, we attempt to simultaneously assemble smaller-sized Ag NPs (8 nm) and larger-sized Au NPs (20 nm) onto BTO nanosheets with nearly 100% exposed (010) facet. The two types of noble metal NPs act, respectively, as electron sinks and LSPR effects, and moreover, it could bring about a synergistic effect between them. This work offers a promising insight for developing photocatalysts with high photocatalytic activity.

2 Experimental

2.1 Assembly of Au and Ag NPs on BTO nanosheets

BTO nanosheets used in this study were synthesized via a hydrothermal route as described in the literature [39]. A photocatalytic reduction route was used to assemble Au and Ag NPs onto the surface of BTO nanosheets. In a typical preparation of Au–Ag@BTO, 0.1 g of BTO nanosheets and 0.05 g of ammonium oxalate(AO) were added in 80 mL deionized water, followed by 30 min of ultrasonic treatment and then 30 min of magnetic stirring. To the suspension was slowly dropped with 0.24 mL of $AgNO_3$ solution (concentration: 0.2 mol L^{-1}) and 0.86 mL of $HAuCl_4$ solution (concentration: 0.029 mol L^{-1}). After magnetically stirred for 60 min, the mixture was irradiated by a 15 W low-pressure mercury lamp emitting UV light under mild magnetic stirring. Under the UV irradiation, electrons were excited from the VB to the CB of BTO. The photogenerated electrons were coupled with Au^{3+} and Ag^+ ions, thus making them reduced to form Au and Ag NPs onto the surface of BTO nanosheets. The involved reactions can be simply described by Eqs. (1)−(3). After 30 min of irradiation, the product was collected and washed with deionized water (three times) and absolute ethanol (one times), followed by drying at 60 °C for 12 h to obtain final Au–Ag@BTO composite.

$$Bi_4Ti_3O_{12} + h\nu \rightarrow Bi_4Ti_3O_{12}\left(e^- + h^+\right) \quad (1)$$

$$Au^{3+} + 3e^- \rightarrow Au_{(metal)} \quad (2)$$

$$Ag^+ + e^- \rightarrow Ag_{(metal)} \quad (3)$$

2.2 Sample characterization

X-ray powder diffraction (XRD) with Cu Kα radiation (λ = 0.15406 nm) was used for the phase identification of the samples on a D8 Advance X-ray diffractometer. The morphology and microstructure of the samples was investigated using transmission electron microscopy (TEM) on a JEM-1200EX transmission electron microscope. Energy-dispersive X-ray spectroscopy (EDS) attached to TEM was used to analyze the chemical composition and elemental distribution of the samples. The chemical states of elements in the samples were determined using X-ray photoelectron

spectroscopy (XPS) on a PHI-5702 multi-functional X-ray photoelectron spectrometer. Fourier transform infrared spectroscopy (FTIR) analysis was carried out on a PerkinElmer Spectrum Two spectrophotometer in the range of 500–4000 cm^{-1} using KBr powder. Ultraviolet–visible diffuse reflectance spectroscopy (UV–vis DRS) was performed on a TU-1901 double beam UV–vis spectrophotometer to characterize the optical absorption and bandgap energy of the samples. A RF-6000 fluorescence spectrophotometer was used to measure the photoluminescence (PL) spectra of the samples (excitation wavelength: 320 nm).

2.3 Photocatalytic experiment

Rhodamine B (RhB) in aqueous solution was chosen as the target organic pollutant to evaluate the photocatalytic activity of the samples for the pollutant abatement. Simulated sunlight emitted from a xenon lamp, UV light ($\lambda = 254$ nm) emitted from a low-pressure mercury lamp and visible light ($\lambda > 400$ nm) generated by a halogen-tungsten lamp were separately used the light source. In a typical photocatalytic experiment, 100 mL of 5 mg L^{-1} RhB aqueous solution and 0.1 g of the photocatalyst were put into the photoreactor (photocatalyst concentration: 1 g L^{-1}). The mixture was magnetically stirred in the dark for 30 min to determine the adsorption of RhB onto the photocatalyst surface. After that, the mixture was irradiated to initiate the photocatalytic reaction. To exclude the thermal effect on the photocatalysis, the reaction solution was maintained at room temperature (21 °C) by cooling the photoreactor with a circulating water cooling system. At intervals of 30 min, 2.5 mL of the reaction solution was sampled from the photoreactor and used to determine the residual concentration of RhB. After removal of the photocatalyst by centrifugation, the absorbance of the reaction solution was measured on a UV–vis spectrophotometer at $\lambda = 554$ nm, from which the residual concentration of RhB was determined. The degradation percentage of RhB is defined as follows: $D\% = (C_0 - C_t)/C_0 \times 100\%$, where C_0 = initial RhB concentration and C_t = residual RhB concentration after t min of photocatalysis. The effects of the RhB concentration and photocatalyst dosage on the photocatalytic degradation of RhB were investigated following the same photocatalytic procedure as described above.

To reveal the role of the reactive species hydroxyl (·OH), superoxide ($\cdot O_2^-$) and photogenerated h^+ in the RhB degradation over the Au–Ag@BTO photocatalyst, ethanol, benzoquinone (BQ) and AO were used as the scavengers of ·OH, $\cdot O_2^-$ and h^+, respectively [40]. In a typical reactive species trapping experiment, 0.1 g of Au–Ag@BTO and 100 mL of 5 mg L^{-1} RhB solution were loaded into the photoreactor. Then an appropriate amount of ethanol (5 mL), BQ (0.1 mmol) and AO (0.1 mmol) were separately added in the mixture. After magnetically stirred in the dark for 30 min, the mixture was irradiated with simulated sunlight from a xenon lamp. The concentration change of RhB during the irradiation was monitored following the same procedure as described above.

2.4 Photocurrent and EIS measurements

Transient photocurrent response and electrochemical impedance spectroscopy (EIS) of the samples were measured on a CST 350 electrochemical workstation. A three-electrode cell configuration composed of the counter electrode (a platinum foil electrode), reference electrode (a standard calomel electrode (SCE)) and working electrode was used to for the photoelectrochemical measurements. The working electrode was prepared following the procedure described in the literature [41]. The photocatalyst, carbon black and polyvinylidene fluoride (PVDF) were uniformly mixed in a mass ratio of 20: 1: 1 using 1-methyl-2-pyrrolidione (NMP) as the dispersant. The formed slurry was dispersed uniformly onto fluorine-doped tin oxide (FTO) glass substrate with an effective area of 1×1 cm^2, followed by drying at 60 °C for 5 h. The effective mass of the photocatalyst on the final working electrode was 15 mg. 0.1 mol L^{-1} Na_2SO_4 aqueous solution was used as the electrolyte. Simulated sunlight emitting from a xenon lamp was used as the light source. A bias potential of 0.2 V was applied during the transient photocurrent response measurement. The EIS measurement was performed by imposing a small sinusoidal voltage of 5 mV amplitude over the frequency range from 100 kHz to 0.01 Hz.

3 Results and discussion

3.1 TEM analysis

Figure 1a shows the TEM image of the Au–Ag@BTO photocatalyst, from which it is seen that the large-sized BTO nanosheet is uniformly decorated with two types of spherical nanoparticles with different sizes. One has an average size of ~ 20 nm and the other has an average size of ~ 8 nm. The two types of nanoparticles are Au and Ag NPs, respectively, as confirmed from the energy-dispersive X-ray elemental mapping images shown in Fig. 2. The high resolution TEM (HRTEM) image (Fig. 1b) demonstrates that the BTO nanosheet and Au/Ag NPs exhibit perfect crystal lattice fringes with no internal defects. The BTO nanosheet shows the lattice fringes with a d-spacing of 0.388 nm, which matches well with the (202) crystal plane of orthorhombic BTO phase. The lattice fringes observed for the larger-sized particle have a d-spacing of 0.236 nm, which correspond to the (111) crystal plane of cubic Au phase. The HRTEM image also reveals good assembly of Au/Ag NPs onto BTO

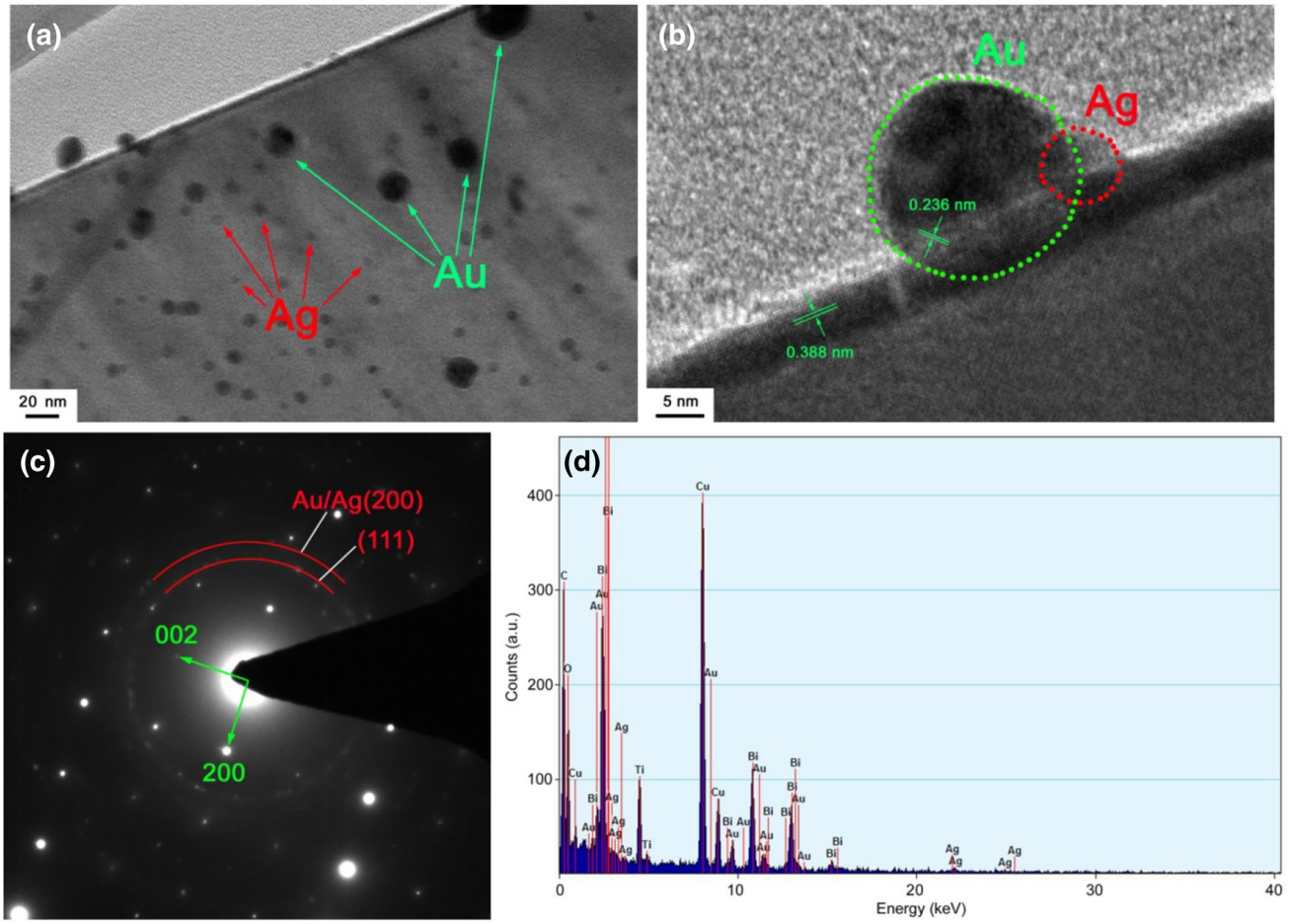

Fig. 1 TEM image (**a**), HRTEM image (**b**), SAED pattern (**c**) and EDS spectrum (**d**) of the Au–Ag@BTO photocatalyst

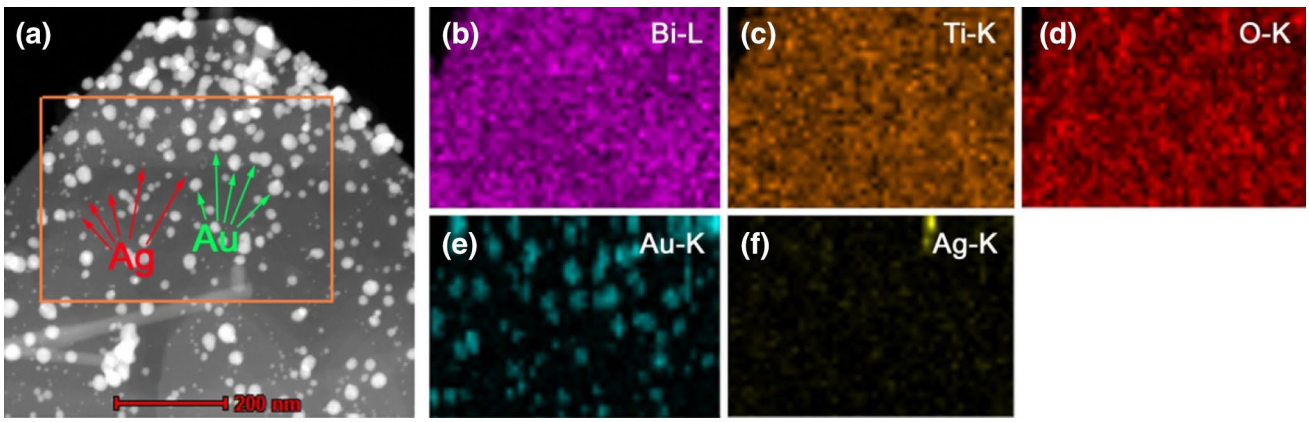

Fig. 2 **a** DF-STEM image of Au–Ag@BTO. **b–f** The corresponding EDS elemental mapping images of the region marked by yellow rectangle in (**c**) (Color figure online)

nanosheets. The crystallization and crystal structure of Au–Ag@BTO was investigated by the selected area electron diffraction (SAED) pattern. As shown in Fig. 1c, the SAED pattern consists of two sets of diffraction spots. One set of diffraction spots are regularly and periodically arranged, which can be indexed to the [010] zone axis of BTO orthorhombic structure. This also implies the highly exposed (010) facet of BTO nanosheets. The other set of diffraction

spots are arranged in continuous concentric Debye rings characteristic for the polycrystalline Au/Ag NPs. No additional diffraction spots or rings assignable to other impurity phases are visible in the SAED pattern. Energy-dispersive X-ray spectroscopy (EDS) was used to analyze the chemical composition of Au–Ag@BTO. The measured EDS spectrum is shown in Fig. 1d, revealing the existence of Bi, Ti, O, Au and Ag elements in the Au–Ag@BTO sample. The observed Cu and C signals could arise from the microgrid used for supporting the sample in the TEM experiment [42]. Based on the EDS spectrum, the obtained Bi/Ti atomic ratio is very close to 4/3, which is in accord with the stoichiometric Bi/Ti atomic ratio in BTO phase. The measured mass fraction of Au and Ag in the composite sample is about 4.2% and 3.9%, respectively. However, the measured O content is much lower than the stoichiometric O content in the BTO phase. This could be attributed to the fact that EDS is not sensitive to light elements like O and is not suitable for the determination of light elements [42].

Figure 2a shows the dark-field scanning TEM (DF-STEM) image of the Au–Ag@BTO composite. It is seen that two types of bright nanoparticles separately with an average size of 20 and 8 nm are uniformly decorated onto the surface of gray lamellar sheet. The corresponding energy-dispersive X-ray elemental mapping images of the region marked by yellow rectangle in Fig. 2a are displayed in Fig. 2b–f. As seen from Fig. 2b–d, the gray lamellar sheet displays the distribution of Bi, Ti and O elements, and is identified to be BTO nanosheet. Figure 2e and f demonstrate that the larger-sized bright nanoparticles on the lamellar sheet consist of Au element, whereas the smaller-sized nanoparticles consist of Ag element. The elemental mapping images further confirm the uniform assembly of two types of nanoparticles, i.e., larger-sized Au NPs (~ 20 nm) and smaller-sized Ag NPs (~ 8 nm), onto the surface of BTO nanosheets.

3.2 XRD analysis

XRD technique was used for the structural determination of the samples. Figure 3 shows the XRD patterns of BTO and Au–Ag@BTO, along with the standard powder XRD patterns of the orthorhombic BTO phase (PDF#35-0795), cubic Au phase (PDF#04-0784) and cubic Ag phase (PDF#04-0783). It is seen that the peak positions and relative intensities of BTO are perfectly in line with the standard pattern of PDF#35-0795, implying that BTO crystallizes in an orthorhombic structure with space group Fmmm (a = 5.45 Å, b = 32.82 Å, a = 5.41 Å). For Au–Ag@BTO, all the diffraction peaks match very well with those of bare BTO, suggesting that BTO undergoes no structural change when decorated with Au and Ag nanoparticles. The most intense diffraction peak of Au and Ag, at around $2\theta = 38.15^{o}$, is overlapped with some diffraction peaks of BTO, as indicated by the arrow. Moreover, Au and Ag account for only a small fraction of the total mass of the Au–Ag@BTO sample. Due to these factors, no obvious diffraction peaks assignable to Au and Ag are visible in the XRD pattern.

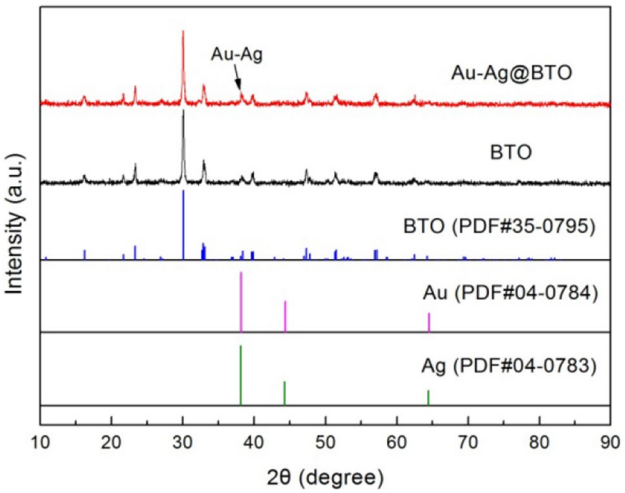

Fig. 3 XRD patterns of BTO and Au–Ag@BTO, along with the standard powder XRD patterns of the orthorhombic BTO phase (PDF#35-0795), cubic Au phase (PDF#04-0784) and cubic Ag phase (PDF#04-0783)

3.3 UV–vis DRS analysis

It is noted that the photocatalytic performances of semiconductors are highly dependent on their optical absorption properties, which can be determined by UV–vis DRS measurements [43]. Figure 4a shows the UV–vis DRS spectra of BTO and Au–Ag@BTO. Compared to BTO, the Au–Ag@BTO composite exhibits significantly enhanced light absorption in the wavelength range of 400−850 nm, which is conducive to the utilization of sunlight during the photocatalysis. The enhanced visible-light absorption of Au–Ag@BTO is further confirmed by the deepening of its apparent color. As demonstrated by the digital images inserted in Fig. 4a, bare BTO is cream white, whereas Au–Ag@BTO exhibits a gray color. Further, an obvious plasmon resonance peak at around 560 nm is observed on the UV–vis DRS spectrum of Au–Ag@BTO. It is generally accepted that the quality factor of the LSP resonance of metal NPs, which is given by the ratio of the resonance frequency to the full width at half-maximum of the peak, is directly proportional to the local electric field enhancement [44]. To derive the absorption edge and bandgap of the samples, the first derivative curves of the UV–vis DRS spectra of the samples are illustrated in Fig. 4b. As seen from Fig. 4b, BTO and Au–Ag@BTO exhibit an absorption edge of 396.5 and 357.7 nm, respectively. Based on the absorption edge, the bandgap energy (E_g) of BTO is obtained as 3.13 eV for bare BTO and

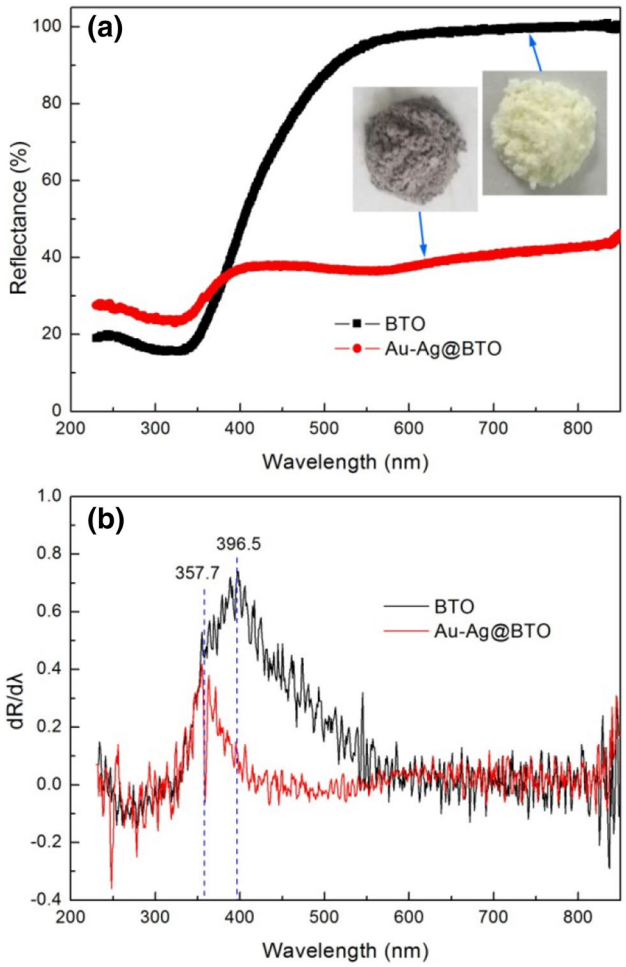

Fig. 4 UV-vis DRS spectra (**a**) and the corresponding first derivative curves (**b**) of BTO and Au–Ag@BTO. The inset in (a) shows the apparent colors of BTO and Au–Ag@BTO

3.47 eV for Au–Ag@BTO. The slight increase in the E_g of the composite could be ascribed to the interaction between BTO nanosheets and Au/Ag NPs.

3.4 XPS analysis

To reveal the chemical states of the elements in Au–Ag@BTO, XPS analysis was carried out and the results are shown in Fig. 5. The XPS survey scan spectrum (Fig. 5a) shows the existence of the elements Bi, Ti, O, Au and Ag in the Au–Ag@BTO composite. Adventitious carbon with C 1s at 284.8 eV is used to calibrate the binding energy scale. The high resolution XPS spectra of Bi 4f, Ti 2p, O 1s, Au 4f and Ag 3d are illustrated in Fig. 5b–f, respectively. As seen from Fig. 5b, the Bi 4f XPS spectrum manifests two sharp peaks separately at 159.2 (Bi $4f_{7/2}$) and 164.5 eV (Bi $4f_{5/2}$) without additional Bi 4f binding energy peaks. This indicates that bismuth species exhibits the oxidation state of Bi^{3+} [27, 45, 46]. The Ti 2p XPS spectrum (Fig. 5c) can be deconvoluted into three peaks at 458.2, 463.8 and 466.2 eV, which are assigned to the binding energies of Ti $2p_{3/2}$, Ti $2p_{1/2}$ and Bi $4d_{3/2}$ respectively [27, 45, 46]. No additional binding energy peaks are visible on the Ti 2p XPS spectrum, implying that titanium species behaves as the Ti^{4+} oxidation state. On the O 1s XPS spectrum (Fig. 5d), the O 1s binding energy of the crystal lattice oxygen of BTO is observed at 530.0 eV [27]. The binding energy at 532.1 eV could arise from chemisorbed oxygen species [27]. The Au 4f XPS spectrum (Fig. 5e) presents two sharp peaks at 84.0 (Au $4f_{7/2}$) and 87.7 eV (Au $4f_{5/2}$), and the Ag 3d XPS spectrum (Fig. 5f) displays two sharp peaks at 368.0 (Ag $3d_{5/2}$) and 374.1 eV (Ag $3d_{3/2}$). The binding energies of Au 4f and Ag 3d suggest that both Au and Ag species are in the form of metal state [47, 48]. The existence of oxidation states of Au and Ag can be excluded since no additional peaks are observed on the spectra.

3.5 FTIR analysis

FTIR analysis was carried out to reveal the functional groups of BTO and Au–Ag@BTO, as shown in Fig. 6. The band peak at 815 cm^{-1} is assigned to the characteristic stretching vibration of Bi–O, whereas the strong peak at 571 cm^{-1} and weak peak at 472 cm^{-1} are attributed to the Ti–O stretching vibration [49, 50]. This implies the formation of BTO orthorhombic phase and its crystal structure undergoes no destruction on the decoration of Au and Ag NPs. The broad bands observed at 1637 and 3430 cm^{-1} arise from the bending and stretching vibrations of water molecules absorbed on the surface of the samples, respectively. The peaks detected at 1098 and 1403 cm^{-1} account for the C–OH stretching and O–H in-plane deformation vibrations of alcohols left on the samples during their washing process. A strong and broad absorption band centered around 3155 cm^{-1} is observed for BTO, which is attributed to the N–H stretching vibration [51]. This indicates that NH^{3+} group could be formed during the hydrothermal synthesis of BTO due to the addition of nitric acid [30]. The N–H vibration band disappears for Au–Ag@BTO, implying that the decoration of Au/Ag NPs on BTO results in the removal of NH^{3+}. In addition, no characteristic peaks assignable to Au and Ag oxides are observed for Au–Ag@BTO, implying Au and Ag species exist in the metallic states.

3.6 Photocatalytic performances

The photocatalytic activity of BTO and Au–Ag@BTO was evaluated by the degradation of RhB in aqueous solution separately under irradiation of simulated sunlight, UV light ($\lambda = 254$ nm) and visible light ($\lambda > 400$ nm). Before the photocatalytic degradation experiment, the adsorption of RhB onto BTO and Au–Ag@BTO was measured in the

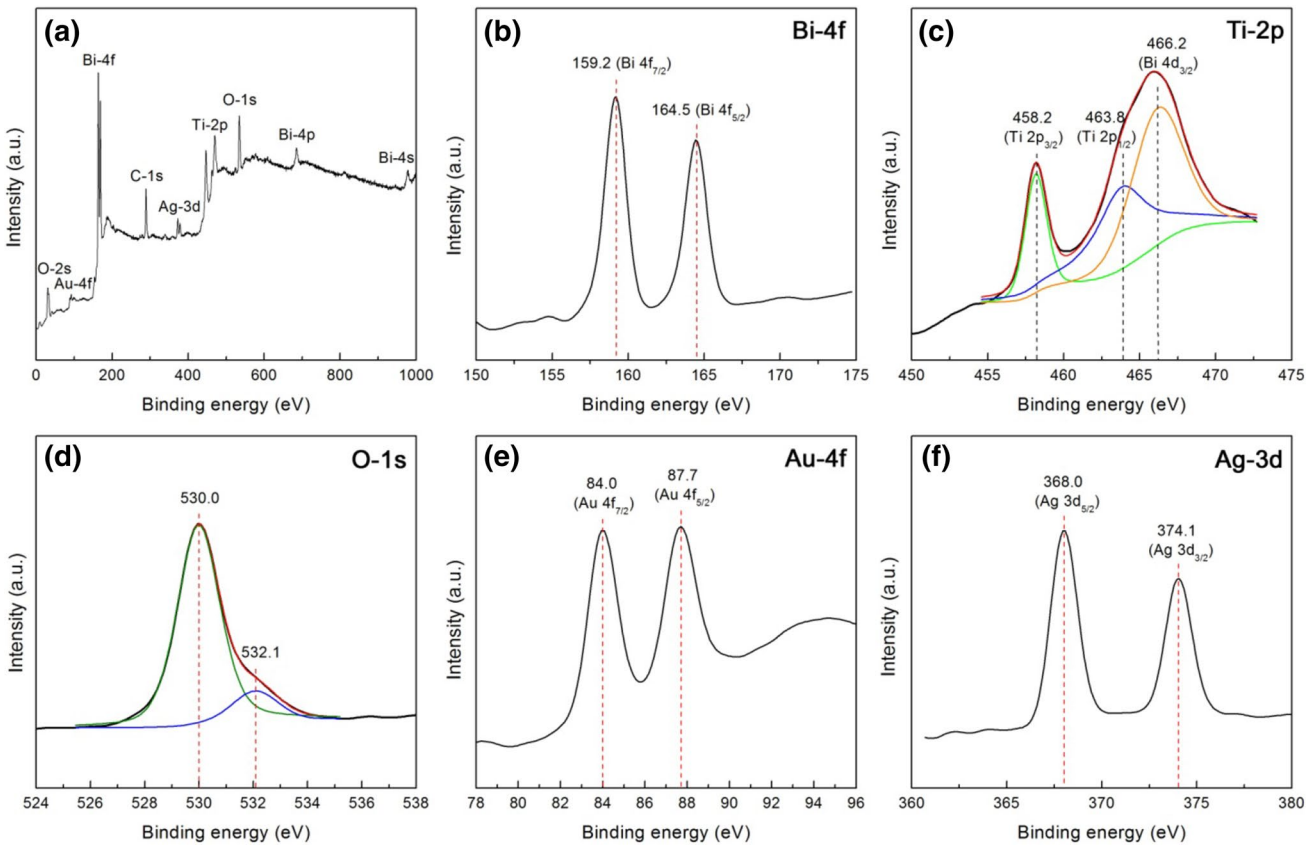

Fig. 5 XPS survey scan spectrum (**a**) and high resolution XPS spectra of **b** Bi 4f, **c** Ti 2p, **d** O 1s, **e** Au 4f and **f** Ag 3d for Au–Ag@BTO

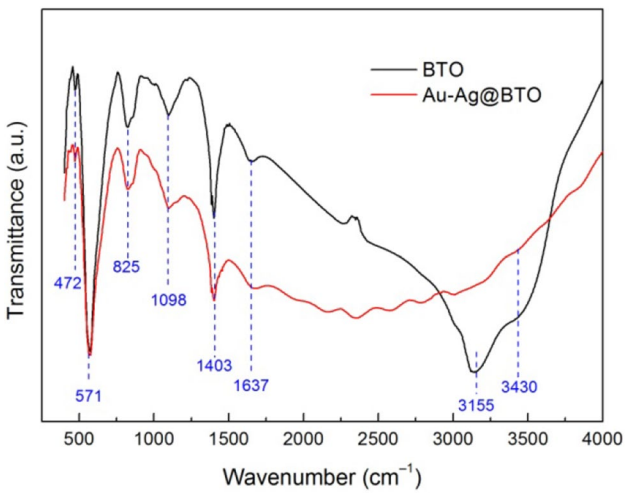

Fig. 6 FTIR spectra of BTO and Au–Ag@BTO

dark at 30 min of contact time, and is obtained as 8.3% and 9.1%, respectively. The time-dependent photocatalytic degradation of RhB under simulated sunlight irradiation is shown in Fig. 7a. Compared to bare BTO nanosheets, Au/Ag NPs decorated BTO nanosheets manifest obviously enhanced photocatalytic activity. After photocatalytic reaction for 120 min, the degradation percentage of RhB over bare BTO is obtained as 74.6%, whereas the dye degradation is increased up to 95.9% catalyzed by Au–Ag@BTO. The apparent first-order reaction rate constant k_{app} of the dye degradation is used to further compare the photocatalytic activity between the samples. Based on the first-order kinetic plots of $\mathrm{Ln}(C_t/C_0)$ *vs* irradiation time t, the value of k_{app} is obtained as 0.01166 min^{-1} for bare BTO and 0.02671 min^{-1} for Au–Ag@BTO, implying that the latter has a photocatalytic activity ca. 2.3 times higher than the former. Figure 7b shows the photocatalytic degradation of RhB over BTO and Au–Ag@BTO under UV irradiation. It is obvious that BTO is an excellent UV active photocatalyst. Moreover, when decorated with Au and Ag NPs, the resultant Au–Ag@BTO manifests a significantly enhanced UV photocatalytic activity compared to bare BTO. The degradation percentage of the dye after 120 min of the UV photocatalysis reaches 97.5% and 99.9% for BTO and Au–Ag@BTO, respectively. The reaction rate constant obtained from first-order kinetic plots ($k_{app(BTO)} = 0.02941$ min^{-1}, $k_{app(Au–Ag@BTO)} = 0.06333$ min^{-1}) suggests that the UV photocatalytic activity of Au–Ag@BTO is ca. 2.2 times as large as that of bare BTO. The visible-light photocatalytic activity

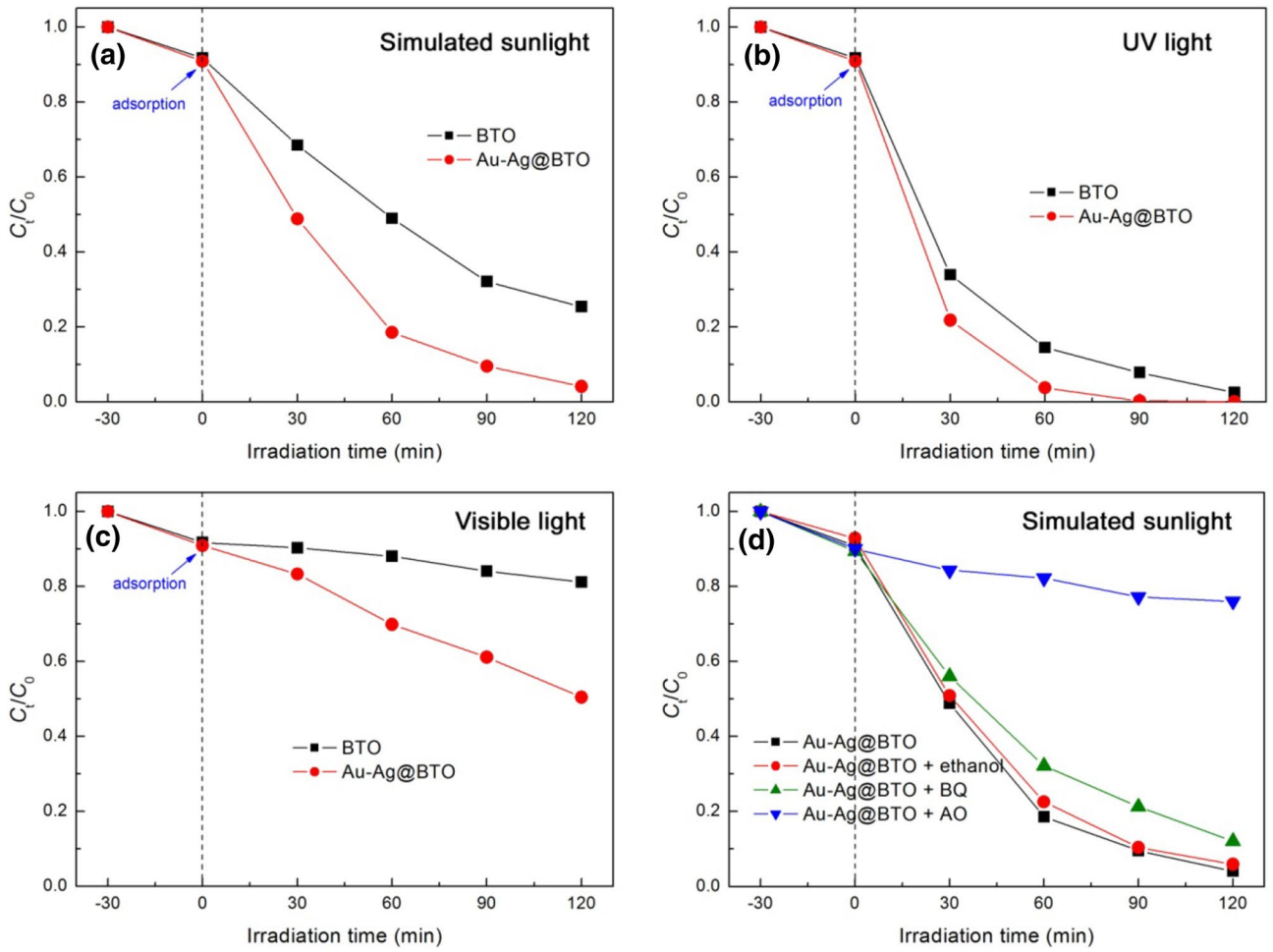

Fig. 7 **a–c** Time-dependent photocatalytic degradation of RhB over BTO and Au–Ag@BTO under irradiation of simulated sunlight, UV light (λ = 254 nm) and visible light (λ > 400 nm), respectively. **d** Effects of ethanol, BQ and AO on the degradation of RhB over Au–Ag@BTO under simulated sunlight irradiation

of the samples toward the RhB degradation is illustrated in Fig. 7c. After irradiation for 120 min, 18.8% and 49.6% of the dye are observed to be degraded photocatalyzed by BTO and Au–Ag@BTO, respectively. This indicates that bare BTO exhibits a poor photocatalytic activity under visible light irradiation, whereas a significantly enhanced visible-light photocatalytic activity is observed for Au–Ag@BTO. The photocatalytic experiments demonstrate that the assembly of Au/Ag NPs onto BTO nanosheets leads to greatly enhanced photocatalytic activity under both UV and visible light irradiation. However, the enhanced photocatalytic mechanism could be different between UV and visible light irradiation, which will be discussed later in the following section. The effect of Au–Ag@BTO dosage on the degradation percentage of RhB after 120 min of simulated sunlight irradiation is illustrated in Fig. S1. The optimal dosage of the photocatalyst is observed to be about 1 g L^{-1}. It is generally accepted that an appropriate increase in photocatalyst dosage can offer more active sites for the photoreaction. However, the excessive loading of photocatalyst will reduce the light transmission and availability, consequently leading to a decrease in the photocatalytic efficiency [52]. The effect of RhB concentration on its degradation is shown in Figure S2. Although the degradation percentage of RhB decreases with increasing the initial RhB concentration, the Au–Ag@BTO composite still photocatalyzes a 56.2% degradation of RhB even at a high RhB concentration of 30 mg L^{-1}.

Reactive species trapping experiments were carried out to reveal the role of ·OH, $\cdot O_2^-$ and h^+ in the photocatalysis. To achieve this aim, ethanol, BQ and AO were respectively used as the scavengers of ·OH, $\cdot O_2^-$ and h^+ [40], and their effects on the degradation of RhB over Au–Ag@BTO under simulated sunlight irradiation are shown in Fig. 7d. It is noticeable that the addition of ethanol has a very small effect on the dye degradation, implying a minor or negligible role of ·OH in the photocatalysis. On the addition of BQ, a slight inhibition of the dye degradation is observed, indicates that $\cdot O_2^-$ plays a slight role in the photocatalytic reaction.

In contrast, the dye degradation is significantly suppressed on the addition of AO and only 23.9% of RhB is observed to be degradation after 120 min of reaction. This indicates that the photogenerated h^+ is the dominant reactive species responsible for the dye degradation.

3.7 Photocurrent and EIS analysis

To reveal the separation and transfer behavior of photogenerated electrons and holes, transient photocurrent response and EIS measurements were carried out. Figure 8a shows the transient photocurrent response curves of BTO and Au–Ag@BTO measured for several on/off cycles of intermittent simulated sunlight irradiation. On the irradiation with simulated sunlight, Au–Ag@BTO manifests a photocurrent density of ca. 1.51−1.72 μA cm^{-2}, whereas only a small photocurrent density of ca. 0.05 μA cm^{-2} is observed for bare BTO. When the light is turned off, the photocurrent density for both samples drops immediately to a very low level. The transient photocurrent measurement clearly demonstrates that Au–Ag@BTO exhibits an enhanced separation of photogenerated electron/hole pairs. This result is further confirmed by the EIS spectra (Nyquist plots), as shown in Fig. 8b. It is clearly seen that the Nyquist plot of Au–Ag@BTO shows a semicircle much smaller than that of bare BTO. It is generally accepted that the semicircle diameter of the Nyquist plots is highly corrected with the charge-transfer resistance at the electrode/electrolyte interface, and a smaller diameter means a smaller charge-transfer resistance [53, 54]. The EIS spectra confirms that Au–Ag@BTO exhibits a greatly enhanced electron/hole pair separation and interface charge transfer under irradiation of simulated sunlight.

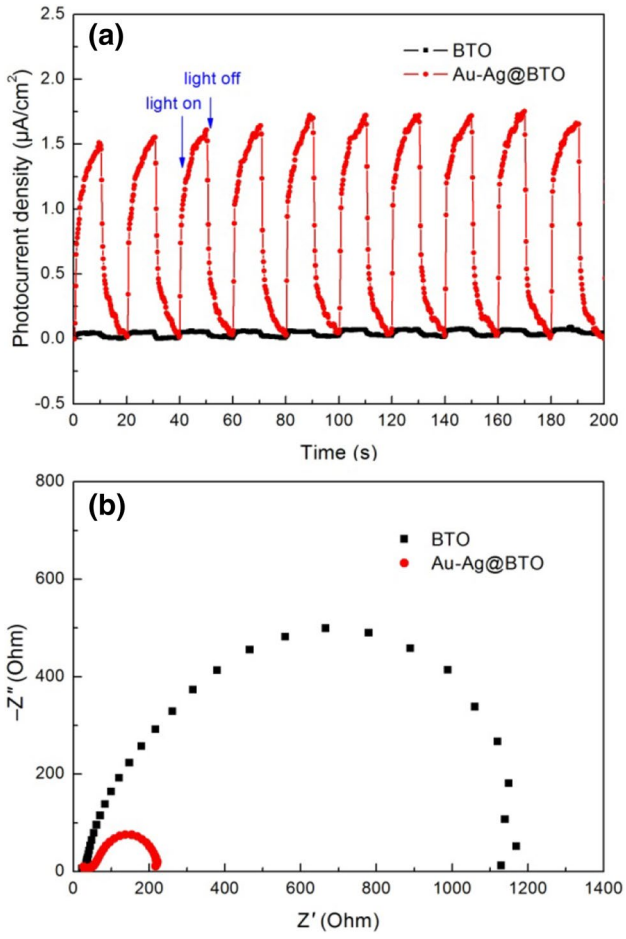

Fig. 8 Transient photocurrent response curves (**a**) and Nyquist plots of the EIS spectra (**b**) for BTO and Au–Ag@BTO

3.8 PL spectrum analysis

PL spectroscopy is another important technique that can be used to determine the charge separation behavior [55]. Figure 9 shows the PL spectra of BTO and Au–Ag@BTO measured at an excitation wavelength of 320 nm. Several PL emission peaks at 448, 466, 480 and 491 nm are clearly observed for both the samples, which could arise from the recombination of photogenerated electrons and holes. However, the PL emission peaks from Au–Ag@BTO have a lower intensity than those from bare BTO, implying a decreased electron/hole recombination occurring in the composite. The efficient separation of electron/hole pairs in the composite is due to the electron transfer from the CB of BTO to Ag NPs. As a result, more photogenerated holes in the Au–Ag@BTO composites are able to participate in the photocatalytic reactions.

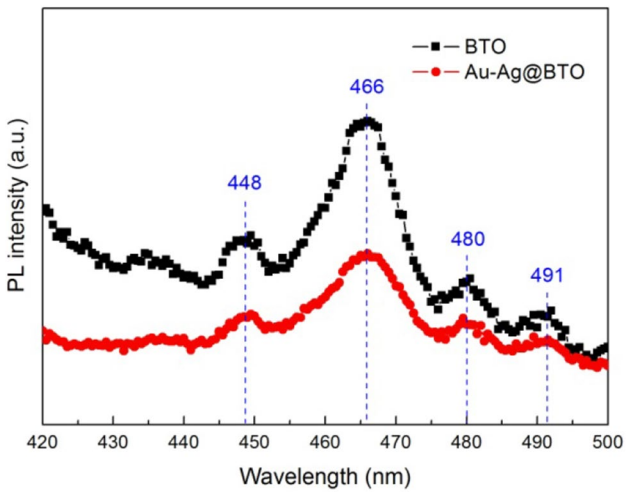

Fig. 9 PL spectra of BTO and Au–Ag@BTO measured at an excitation wavelength of 320 nm

3.9 Photocatalytic mechanism

Based on the aforementioned experimental results and analysis, a possible photocatalytic degradation mechanism of the dye over Au–Ag@BTO is proposed, as schematically illustrated Fig. 10. In the presently synthesized Au–Ag@BTO composite, two types of noble metal NPs with different sizes, i.e., smaller-sized Ag NPs (8 nm) and larger-sized Au NPs (20 nm), are assembled on the surface of BTO nanosheets. It is generally accepted that noble metal NPs can be used as excellent electron sinks to capture photogenerated electrons. However, as the size of noble metal NPs increases, particularly up to 20−25 nm, their LSPR effects become more important [56–58]. Therefore, the smaller-sized Ag NPs and larger-sized Au NPs are expected to behave mainly as electron sinks and LSPR effects in the Au–Ag@BTO photocatalyst, respectively. Under simulated sunlight irradiation, electrons are excited from the CB of BTO to its VB, thus creating electron/hole pairs. Considering that the Fermi level of Ag (+0.4 V *vs* normal hydrogen electrode (NHE) [59]) is more positive than the CB potential of BTO (−0.10 V vs. NHE [27]), the photogenerated electrons will be transferred spontaneously from the CB of BTO to the Ag NPs. This electron transfer process promotes the space-charge separation of the electron/hole pairs in BTO, and as a result, the holes in the VB of BTO will have a longer lifetime to participate in the photocatalytic reactions. On the other hand, Au NPs generate intense LSPR under irradiation of simulated sunlight. The strongly enhanced electric field induced by the plasmonic Au NPs can stimulate the interband excitation in BTO and facilitate the separation of electron/hole pairs [22, 23]. This is the dominant mechanism for the photocatalytic enhancement by the plasmonic Au NPs. Moreover, the Au NPs can be also excited by LSPR to generate electrons and holes [22, 23]. The electrons LSPR-generated in the Au NPs will be fed into the CB of BTO or Ag NPs. Whereas the holes generated in the plasmonic Au NPs could participate in the oxidation reactions. However, the oxidation reactions will be mild or partially take place, because the generated holes in Au NPs do not have a strong oxidation potential. All these factors collectively contribute to the enhanced photocatalytic performance of Au–Ag@BTO under simulated sunlight irradiation. Under UV irradiation, the photocatalytic enhancement is mainly ascribed to the efficient separation of photogenerated electron/hole pairs caused by the smaller-sized Ag NPs, whereas the photocatalytic enhancement under visible light irradiation is dominantly due to the LSPR effects of the larger-sized Au NPs. The synergistic effect between Ag NPs and Au NPs is achieved under simulated sunlight irradiation.

In most of the photocatalysts, ·OH radicals are confirmed to be the dominant active species responsible for the dye gradation. From a thermodynamic point of view, ·OH radicals are expected to be generated by the reaction of the VB holes in BTO with OH^- or H_2O since the VB potential of BTO (+3.13 V vs. NHE) is more positive than the redox potentials of H_2O/·OH (+2.38 V vs. NHE) and OH^-/·OH (+1.99 V vs. NHE) [60]. However, the reactive species trapping experiments demonstrate that ·OH plays a minor role in the dye degradation. Furthermore, no ·OH radicals are detected in the Au–Ag@BTO photocatalytic system by photoluminescence spectroscopy using terephthalic acid as a probe of ·OH as described in the literature [60]. Photogenerated holes are determined to be the dominant reactive species according to the reactive species trapping experiments. In addition, the role of $\cdot O_2^-$ can not be neglected, but it plays only a slight role in the photocatalytic reaction. The generation of $\cdot O_2^-$ radicals could be derived from the reaction of adsorbed O_2 molecules with the LSPR-induced electrons in Au NPs or photogenerated electrons at higher excited states of BTO.

3.10 Reusability of Au–Ag@BTO

The reusability of the Au–Ag@BTO photocatalyst for the photocatalytic degradation of RhB was investigated by the recycling experiment. The photocatalyst was collected when

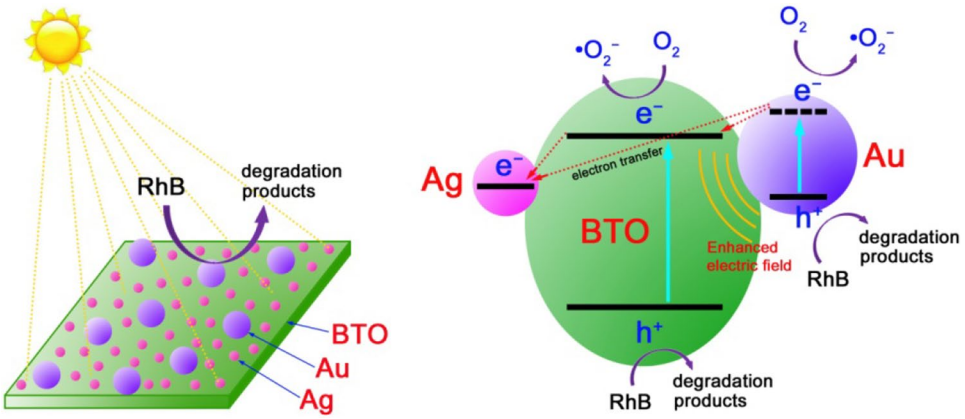

Fig. 10 Schematic illustration of the photocatalytic mechanism of Au–Ag@BTO for the dye degradation under simulated sunlight irradiation

the photocatalysis process was completed. After washing with deionized water and drying at 60 °C for 5 h, the recovered photocatalyst was loaded into 100 mL fresh RhB solution. The photocatalytic experiment was performed under the same conditions of the first photocatalytic cycle. As shown in Fig. 11a, the degradation percentage of RhB at the 4th cycle of the photocatalysis still maintains a high level of 87.7% after reaction for 120 min, indicating an excellent photocatalytic stability of Au–Ag@BTO toward the dye degradation. The crystal structure and microstructure of Au–Ag@BTO after being repeatedly used for four times were also examined by TEM and XRD, as shown in Fig. 11b. It is seen that the diffraction peaks of photocatalytically used Au–Ag@BTO are very similar to those of unused sample, implying that the crystal structure of the composite undergoes almost no change. The TEM image (inset in Fig. 10b) shows that Au and Ag NPs are uniformly decorated onto the surface of BTO nanosheets without obvious destruction of the composite structure.

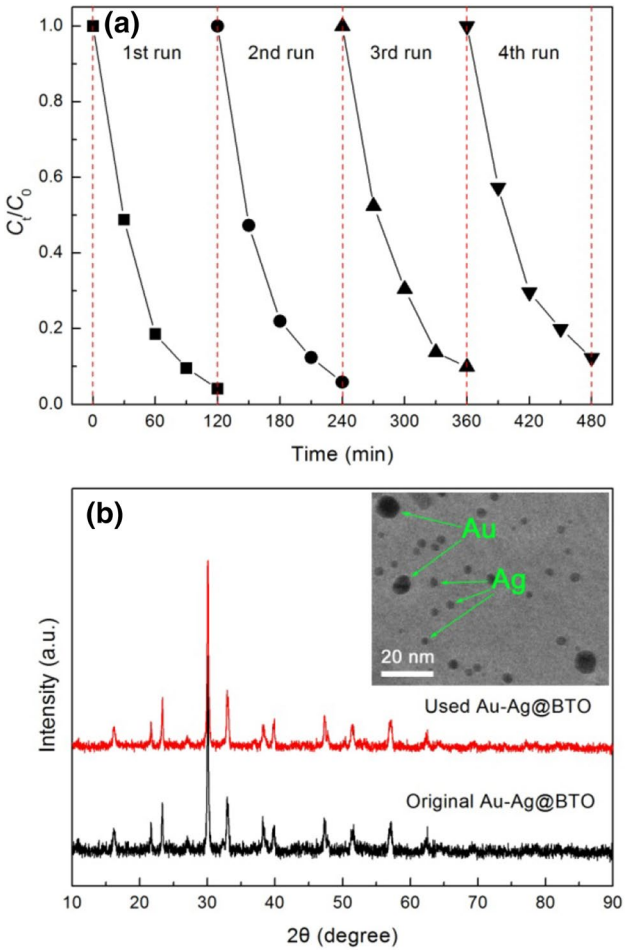

Fig. 11 **a** Reusability of Au–Ag@BTO for the photocatalytic degradation of RhB under simulated sunlight irradiation. **b** XRD patterns of Au–Ag@BTO before and after repeatedly used for four times. The inset shows the TEM image of the used Au–Ag@BTO

4 Conclusions

Two types of noble metal NPs, i.e. larger-sized Au NPs with an average diameter of 20 nm and smaller-sized Ag NPs with an average diameter of 8 nm, were uniformly assembled on the surface of BTO nanosheets. Compared to bare BTO, the as-prepared Au–Ag@BTO composite exhibits an increased photocatalytic performance for the dye degradation under irradiation of simulated sunlight, UV light and visible light. The Au and Ag NPs play different mechanisms for the enhanced photocatalytic performance of the composite. The smaller-sized Ag NPs mainly act as electron sinks to promote the separation of photogenerated electron/hole pairs, thus leading to the enhanced UV photocatalytic performance. The larger-sized Au NPs dominantly behave as LSPR effects to enhance the visible light photocatalytic performance. A synergistic effect between Ag and Au NPs for the enhanced photocatalytic performance is achieved under simulated sunlight irradiation. Based on the active species trapping experiments, photogenerated holes and $\cdot O_2^-$ radicals are suggested to be the dominant and secondary reactive species in the photocatalysis, respectively. Moreover, the Au–Ag@BTO composite exhibits a good photocatalytic stability and could find a promising application in wastewater treatment.

Acknowledgements This work was supported by the National Natural Science Foundation of China (Grant No. 51662027) and the HongLiu First-Class Disciplines Development Program of Lanzhou University of Technology.

References

1. A.R. Khataeea, M.B. Kasiri, J. Mol. Catal. A **328**, 8 (2010)
2. P. Moroz, A. Boddy, M. Zamkov, Front. Chem. **6**, 353 (2018)
3. S.G. Kumar, K.S.R.K. Rao, Appl. Surf. Sci. **391**, 124 (2017)
4. L.J. Di, H. Yang, T. Xian, X.J. Chen, Micromachines **9**, 613 (2018)
5. Z.M. He, Y.M. Xia, B. Tang, X.F. Jiang, J.B. Su, Mater. Lett. **184**, 148 (2016)
6. R. Daghrir, P. Drogui, D. Robert, Ind. Eng. Chem. Res. **52**, 3581 (2013)
7. Z. He, X.Y. Sun, X. Gu, J. Mater. Sci. **28**, 13950 (2017)
8. Y.X. Yan, H. Yang, X.X. Zhao, H.M. Zhang, J.L. Jiang, J. Electron. Mater. **47**, 3045 (2018)
9. Z. Chen, H. Jiang, W. Jin, C. Shi, Appl. Catal. B **180**, 698 (2016)
10. X.X. Zhao, H. Yang, R.S. Li, Z.M. Cui, X.Q. Liu, Environ. Sci. Pollut. Res. **26**, 5524 (2019)
11. Y.M. Xia, Z.M. He, Y.L. Lu, B. Tang, S.P. Sun, J.B. Su, X.P. Li, RSC Adv. **8**, 5441 (2018)
12. Y. Zeng, X.F. Chen, Z. Yi, Y.G. Yi, X.B. Xu, Appl. Surf. Sci. **441**, 40 (2018)

13. Y.X. Yan, H. Yang, X.X. Zhao, R.S. Li, X.X. Wang, Mater. Res. Bull. **105**, 286 (2018)
14. L. Liu, J.J. Chen, Z.G. Zhou, Z. Yi, X. Ye, Mater. Res. Express **5**, 045802 (2018)
15. J. Huang, G. Niu, Z. Yi, X.F. Chen, Z.G. Zhou, X. Ye, Y.J. Tang, T. Duan, Y. Yi, Y.G. Yi, Phys. Scr. (2019). https://doi.org/10.1088/1402-4896/ab185f
16. Z. Yi, L. Liu, L. Wang, C. Cen, X. Chen, Z. Zhou, X. Ye, Y. Yi, Y. Tang, Y. Yi, P. Wu, Results Phys. **13**, 102217 (2019)
17. X.X. Wang, J.K. Zhu, H. Tong, X.D. Yang, X.X. Wu, Z.Y. Pang, H. Yang, Y.P. Qi, Chin. Phys. B **28**, 044201 (2019)
18. X.X. Wang, X.L. Bai, Z.Y. Pang, J.K. Zhu, Y. Wu, H. Yang, Y.P. Qi, X.L. Wen, Opt. Mater. Express **9**, 1872 (2019)
19. H. Adamu, P. Dubey, J.A. Anderson, Chem. Eng. J. **284**, 380 (2016)
20. T. Soltani, A. Tayyebi, B.K. Lee, J. Environ. Manage. **232**, 713 (2019)
21. S.P. Li, X.B. Bian, J.Z. Gao, G.Q. Zhu, M. Hojamberdiev, C.H. Wang, X.M. Wei, J. Mater. Sci. **28**, 17896 (2017)
22. J.E. Lee, S. Bera, Y.S. Choi, W.I. Lee, Appl. Catal. B **214**, 15 (2017)
23. P. She, K.L. Xu, S. Zeng, Q.R. He, H. Sun, Z.N. Liu, J. Colloid Interfaces Sci. **499**, 76 (2017)
24. X.X. Wang, X.X. Wu, J.K. Zhu, Z.Y. Pang, H. Yang, Y.P. Qi, Sensors **19**, 1187 (2019)
25. A.P. Manuel, A. Kirkey, N. Mahdi, K. Shankar, J. Mater. Chem. C **7**, 1821 (2019)
26. X.X. Wang, X.L. Bai, Z.Y. Pang, H. Yang, Y.P. Qi, Results Phys. **12**, 1866 (2019)
27. X.X. Zhao, H. Yang, S.H. Li, Z.M. Cui, C.R. Zhang, Mater. Res. Bull. **107**, 180 (2018)
28. Y.Z. Zhang, Z.W. Chen, Z.Y. Lu, Nanomaterials **8**, 261 (2018)
29. K. Qian, Z.F. Jiang, H. Shi, W. Wei, C.Z. Zhu, J.M. Xie, Mater. Lett. **183**, 303 (2016)
30. X.X. Zhao, H. Yang, Z.M. Cui, X.X. Wang, Z. Yi, Micromachines **10**, 66 (2019)
31. D.F. Hou, X.L. Hu, P. Hu, W. Zhang, M.F. Zhang, Y.H. Huang, Nanoscale **5**, 9764 (2013)
32. Y.B. Liu, G.Q. Zhu, J.Z. Gao, M. Hojamberdiev, H.B. Lu, R.L. Zhu, X.M. Wei, P. Liu, J. Alloy. Compd. **688**, 487 (2016)
33. W. Zhao, H.X. Wang, X.N. Feng, W.Y. Jiang, D. Zhao, J.Y. Li, Mater. Res. Bull. **70**, 179 (2015)
34. C.X. Zheng, H. Yang, Z.M. Cui, H.M. Zhang, X.X. Wang, Nanoscale Res. Lett. **12**, 608 (2017)
35. S.E. Cummins, L.E. Cross, J. Appl. Phys. **39**, 2268 (1968)
36. D.P. Dutta, A.K. Tyagi, Mater. Res. Bull. **74**, 397 (2016)
37. N. Li, J.J. Wu, H.B. Fang, X.H. Zhang, Y.Z. Zheng, X. Tao, Appl. Surf. Sci. **448**, 41 (2018)
38. Y.B. Liu, G.Q. Zhu, J.Z. Gao, M. Hojamberdiev, R.L. Zhu, X.M. Wei, Q.M. Guo, P. Liu, Appl. Catal. B **200**, 72 (2017)
39. X.X. Zhao, H. Yang, H.M. Zhang, Z.M. Cui, W.J. Feng, Desalin. Water Treat. **145**, 326 (2019)
40. L.J. Di, H. Yang, T. Xian, X.J. Chen, Nanoscale Res. Lett. **13**, 257 (2018)
41. H.J. Gao, F. Wang, S.F. Wang, X.X. Wang, Z. Yi, H. Yang, Mater. Res. Bull. **115**, 140 (2019)
42. C.X. Zheng, H. Yang, J. Mater. Sci. **29**, 9291 (2018)
43. Z. Yi, J. Huang, C.L. Cen, X.F. Chen, Z.G. Zhou, Y.J. Tang, B.Y. Wang, Y.G. Yi, J. Wang, P.H. Wu, Results Phys. (2019). https://doi.org/10.1016/j.rinp.2019.102367
44. S. Farsinezhad, S.P. Banerjee, B.B. Rajeeva, B.D. Wiltshire, H. Sharma, A. Sura, A. Mohammadpour, P. Kar, R. Fedosejevs, K. Shankar, ACS Appl. Mater. Interfaces **9**, 740 (2017)
45. M. Pooladi, H. Shokrollahi, S.A.N.H. Lavasani, H. Yang, Mater. Chem. Phys. **229**, 39 (2019)
46. C. Du, D.H. Li, Q.Y. He, J.M. Liu, W. Li, G.N. He, Y.Z. Wang, Phys. Chem. Chem. Phys. **18**, 26530 (2016)
47. Y.X. Yan, H. Yang, Z. Yi, R.S. Li, X.X. Wang, Micromachines **10**, 254 (2019)
48. Y.L. Mikhlin, G.A. Palyanova, Y.V. Tomashevich, E.A. Vishnyakova, S.A. Vorobyev, K.A. Kokh, J. Phys. Chem. Solids **116**, 292 (2018)
49. R.S. Ganesh, S.K. Sharma, N. Abinnas, E. Durgadevi, P. Raji, S. Ponnusamy, C. Muthamizhchelvan, Y. Hayakawa, D.Y. Kim, Mater. Chem. Phys. **192**, 274 (2017)
50. J.A. Dias, J.A. Oliveira, C.G. Renda, M.R. Morelli, Mater. Res. **21**, e20180118 (2018)
51. B.D. Mert, M.E. Mert, G. Kardas, B. Yazici, Appl. Surf. Sci. **258**, 9668 (2012)
52. L.J. Di, H. Yang, T. Xian, X.Q. Liu, X.J. Chen, Nanomaterials **9**, 399 (2019)
53. M.D. Stoller, S.J. Park, Y.W. Zhu, J.H. An, R.S. Ruoff, Nano Lett. **8**, 3498 (2008)
54. Z.M. He, Y.M. Xia, J.B. Su, RSC Adv. **8**, 39187 (2018)
55. S.Y. Wang, H. Yang, X.X. Wang, W.J. Feng, J. Electron. Mater. **48**, 2067 (2019)
56. X.X. Wang, H. Tong, Z.Y. Pang, J.K. Zhu, X.X. Wu, H. Yang, Y.P. Qi, Opt. Quant. Electron. **51**, 38 (2019)
57. Y.B. Zhang, C.L. Cen, C.P. Liang, Z. Yi, X.F. Chen, Y.J. Tang, T. Yi, Y.G. Yi, W. Luo, S.Y. Xiao, Plasmonics (2019). https://doi.org/10.1007/s11468-019-00956-3
58. L.W. Zhang, L.O. Herrmann, J.J. Baumberg, Sci. Rep. **5**, 16660 (2015)
59. P.V. Kamat, J. Phys. Chem. C **111**, 2834 (2007)
60. Y.C. Ye, H. Yang, H.M. Zhang, J.L. Jiang, Environ. Technol. (2018). https://doi.org/10.1080/09593330.2018.1538261